Extracting energy from a flow: An asymptotic approach using vortex-induced vibrations and feedback control

Philippe Meliga [a,*], Jean-Marc Chomaz [b], François Gallaire [a]

[a] LFMI, Ecole Polytechnique Federale de Lausanne, CH-1015 Lausanne, Switzerland
[b] LadHyX, CNRS-Ecole Polytechnique, 91128 Palaiseau, France

A R T I C L E   I N F O

A B S T R A C T

This paper considers vortex-induced vibrations of a cylinder in water streams for renewable energy production. We use an analytical model recently obtained by the authors from the asymptotic analysis of a coupled flow-cylinder system, and assess the ability of a control velocity applied at the cylinder wall to optimize the magnitude of dissipated energy at disposal to be harvested. The retained approach is that of proportional feedback control. When the system evolves on its limit cycle, we show that the control yields an increase in the mean dissipated energy by 3.5%, as well as a significant improvement of the robustness with respect to small inaccuracies of the structural parameters. However, we also show that the system is susceptible to converge to cycles of lower energy when subjected to external disturbances, as a result of the simultaneous existence of multiple stable cycles. Consequently, we propose a transient control algorithm meant to force the return of the system to its optimal cycle. Its efficiency is assessed for two feedback approaches relying on distinct types of measurements: we find significant differences in the time needed to reach convergence to the optimal cycle, which ultimately results in energy being spent when feedback is designed from cylinder measurements, and in energy being harnessed when feedback is designed from flow measurements.

© 2011 Elsevier Ltd. All rights reserved.

1. Introduction

Numerous studies have been devoted to the problem of the flow past a fixed cylinder. It is now well established that the flow undergoes a global instability responsible for the onset of the time-periodic vortex-shedding phenomenon (Mathis et al., 1984). This causes the cylinder to experience unsteady lift and drag forces. If mounted on elastic supports, the cylinder generally undergoes vortex-induced vibrations (VIVs)—see Williamson and Govardhan (2004), Sarpkaya (2004) and Gabbai and Benaroya (2005) for reviews of the recent progress achieved in this field. Whilst the norm is to avoid such synchronization regimes, we examine here the opposite problem of promoting the vortex-induced vibrations of a cylinder in water streams in the perspective of renewable energy production. For instance, electrical energy will be produced if the oscillation of the cylinder periodically displaces a magnet inside a coil. The energy production device induces a structural damping term in the equation governing the motion of the cylinder, the underlying idea being that the energy dissipated by structural damping is at disposal to be harvested. Such an approach is physically tractable and has potentially practical applications. As an example, the *VIVACE* converter is currently being designed to convert hydrokinetic energy into a usable form of energy by enhancing the vortex-induced vibrations of an array of cylinders (Bernitsas et al., 2008, 2009).

---

* Corresponding author.
  E-mail address: philippe.meliga@l3m.univ-mrs.fr (P. Meliga).

Following this line of thought, our objective is to assess the ability of flow control techniques to optimize the magnitude of dissipated energy. The dynamics of the coupled flow-cylinder system is described using the asymptotic model recently derived by Meliga and Chomaz (2011). The main advantage of this approach, which is valid rigorously for small departures from the instability threshold and small cylinder displacements, lies in the fact that the description of the flow dynamics does not resort to empirical modelling but to an exact asymptotic analysis of the Navier–Stokes equations. Moreover, it defines a dominant balance justifying to treat the cylinder as being fixed at leading-order, so that no specific treatment is required in the numerics to take into account the motion of the cylinder boundary.

The coupled system is forced by a control velocity externally applied at the cylinder wall. The retained approach is that of a linear feedback control designed from appropriate measurements of either the cylinder or the flow motion. The motivation is twofold: we aim first at optimizing the orbit of the limit cycle reached by the system at large times in order to maximize the energy gain, i.e. the difference between the mean dissipated energy and the mean kinetic energy expended for control purposes. To this end, we use Lagrangian optimization, that has been very successful in recent applications including transition control in channel flows (Gunzburger, 1997; see Kim and Bewley, 2007 for a review). Owing to the existence of multiple stable cycles at the conditions of optimal feedback, we also design a transient control algorithm meant to force the convergence of the system to the cycle yielding the largest energy gain.

2. An asymptotic model for VIVs at low Reynold numbers

This section is devoted to the presentation of the nonlinear model recently developed by the authors to investigate the vortex-induced vibrations of a rigid circular cylinder (Meliga and Chomaz, 2011). The objective is to review the fundamental physical features of the model, as well as the main technical points underlying its derivation. Readers interested in any additional detail are referred to the original article. The configuration shown in Fig. 1 consists in a cylinder mounted on springs oriented in the crossflow direction. The flow motion is governed by the incompressible Navier–Stokes equations, whereas the cylinder motion is a simple translation governed by a linear mass-damper-spring equation affected by the fluid loading. This yields four parameters of interest, namely the Reynolds number, built here from the cylinder diameter and the free-stream velocity, the dimensionless natural frequency of the cylinder in vacuum ω_s, its structural damping coefficient γ, and the mass ratio m defined as the ratio of the solid to the fluid densities.

2.1. Dominant balance and coupled amplitude equations

The approach proposed by Meliga and Chomaz (2011) consists in an asymptotic expansion of the coupled flow-cylinder system, in terms of a small parameter ϵ representing the order of magnitude of the flow disturbances. At each successive order in ϵ, this requires to solve for flow disturbances $\boldsymbol{q_i} = (\boldsymbol{u_i}, p_i)^{\mathrm{T}}$ ($\boldsymbol{u_i}$ being the velocity and p_i being the pressure), and for the displacements y_i of the cylinder's center of mass.

The expansion is carried out near the threshold of instability of the steady cylinder, found to be $\mathrm{Re}_* = 46.6$, consistently with the threshold value $\mathrm{Re}_* \sim 47$ generally acknowledged in the literature. The key point is the definition of a non-trivial dominant balance producing all effects at the same order, so that the obtained equations are the most general possible. On the one hand, the flow part of the balance assumes that a departure in the Reynolds number Re at order ϵ^2 and a cylinder motion at order ϵ^3 force flow disturbances of order ϵ to grow over a time scale of order $1/\epsilon^2$. The leading-order flow and cylinder variables are modulated by envelopes evolving on the *slow* time scale $T = \epsilon^2 t$ according to

$$\boldsymbol{q}_1 = \epsilon A(T)\hat{\boldsymbol{q}}_{1*}e^{i\omega_* t} + \text{c.c.}, \quad y_3 = \epsilon^3 Y(T)e^{i\omega_* t} + \text{c.c.} \tag{1}$$

In (1), $\hat{\boldsymbol{q}}_1 = (\hat{\boldsymbol{u}}_{1*}, \hat{p}_{1*})^{\mathrm{T}}$ is the marginally stable eigenmode of frequency $\omega_* \sim 0.74$ classically computed from the flow past a fixed cylinder ((Barkley, 2006, among others), A and Y are unknown complex amplitudes depending only on the slow time,
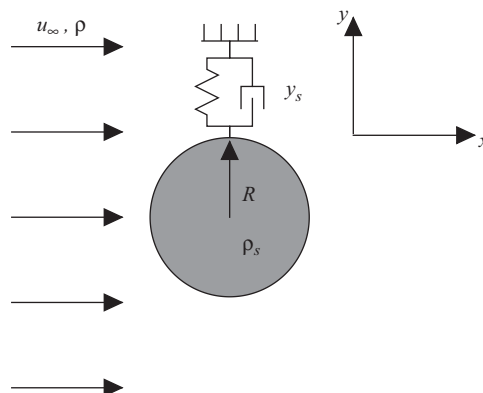
Fig. 1. Schematic of the flow-cylinder configuration.

and c.c. denotes the complex conjugate. On the other hand, the structure part of the balance assumes a large mass ratio of order $1/\epsilon^4$, at the same time with a detuning and a structural damping of order ϵ^2, which puts all inertial, restoring and damping forces in balance with the fluctuating lift force in the structure equation at order ϵ^5.

The model ultimately results from a compatibility condition applied at order ϵ^3, whose role is to guarantee the existence of a solution to the expansion. One obtains in return a system of amplitude equations, i.e. first-order differential equations of polynomial form, governing the time-evolution of the complex amplitudes $\mathcal{A} = \epsilon A$ and $\mathcal{Y} = \epsilon^3 Y$ of the form

$$\frac{\mathrm{d}\mathcal{A}}{\mathrm{d}t} = \lambda\left(\frac{1}{\mathrm{Re}_*} - \frac{1}{\mathrm{Re}}\right)\mathcal{A} - \mu\mathcal{A}|\mathcal{A}|^2 + \alpha\mathcal{Y}, \tag{2a}$$

$$\frac{\mathrm{d}\mathcal{Y}}{\mathrm{d}t} = [-\omega_*\gamma + \mathrm{i}(\omega_s - \omega_*)]\mathcal{Y} + \frac{\beta}{\omega_* m}\mathcal{A}. \tag{2b}$$

Owing to the retained balance, it can be checked that all terms in (2a) are of the same order ϵ^3, whereas all terms in (2b) are of order ϵ^5. The flow disturbances and the cylinder, therefore, behave as a coupled system of oscillators mutually forced near-resonance and amplifying their respective forcing by a factor $1/\epsilon^2$, hence corresponding to a strong coupling. Taking the real and imaginary parts of (2) allows to recast the governing equations into an equivalent three-dimensional polar form for the real amplitudes $|\mathcal{A}|$, $|\mathcal{Y}|$ and the phase $\phi = \arg(\beta\mathcal{A}/\mathcal{Y})$ representing the phase shift between the lift fluctuations and the cylinder displacement:

$$\frac{\mathrm{d}|\mathcal{A}|}{\mathrm{d}t} = \lambda_\mathrm{r}\left(\frac{1}{\mathrm{Re}_*} - \frac{1}{\mathrm{Re}}\right)|\mathcal{A}| - \mu_\mathrm{r}|\mathcal{A}|^3 + |\alpha|\cos(\phi - \phi_\alpha)|\mathcal{Y}|, \tag{3a}$$

$$\frac{\mathrm{d}|\mathcal{Y}|}{\mathrm{d}t} = -\omega_*\gamma|\mathcal{Y}| + \frac{\beta}{\omega_* m}\cos\phi|\mathcal{A}|, \tag{3b}$$

$$(1 + \tan^2\phi)\frac{\mathrm{d}\phi}{\mathrm{d}t} = \mathcal{F}_3\tan^3\phi + \mathcal{F}_2\tan^2\phi + \mathcal{F}_1\tan\phi + \mathcal{F}_0 = 0, \tag{3c}$$

with $\mathcal{F}_m$ ($m = 0 \dots 3$) the real coefficients

$$\begin{aligned}
&\mathcal{F}_3 = -\omega_*\gamma, &&\mathcal{F}_1 = \mathcal{F}_3 - \frac{\beta}{\omega_*^2\gamma m}\left(\alpha_\mathrm{r} + \frac{\mu_\mathrm{i}}{\mu_\mathrm{r}}\alpha_\mathrm{i}\right), \\
&\mathcal{F}_2 = \left(\lambda_\mathrm{i} - \frac{\mu_\mathrm{i}}{\mu_\mathrm{r}}\lambda_\mathrm{r}\right)\left(\frac{1}{\mathrm{Re}_*} - \frac{1}{\mathrm{Re}}\right) - \omega_s + \omega_*, &&\mathcal{F}_0 = \mathcal{F}_2 + \frac{\beta}{\omega_*^2\gamma m}\left(\alpha_\mathrm{i} - \frac{\mu_\mathrm{i}}{\mu_\mathrm{r}}\alpha_\mathrm{r}\right).
\end{aligned} \tag{4}$$

The original form (2) is more suitable to investigate the transient dynamics, where all quantities evolve in time, whereas the recast form (3) is more suitable to investigate the large time dynamics. To facilitate the reading, both forms are alternatively written in compact form as

$$\frac{\mathrm{d}\mathbf{Q}}{\mathrm{d}t} = \mathbf{M}(\mathbf{Q}), \tag{5}$$

with $\mathbf{M}$ the nonlinear evolution operator and $\mathbf{Q}$ the state vector defined as either $\mathbf{Q} = (\mathcal{A}, \mathcal{Y})^\mathrm{T}$ or $\mathbf{Q} = (|\mathcal{A}|, |\mathcal{Y}|, \phi)^\mathrm{T}$, where the choice will be clear from the context.

We assume here a complete knowledge of all flow solutions, including the adjoint of the marginally stable eigenmode denoted $\hat{\boldsymbol{q}}_1^\dagger = (\hat{\boldsymbol{u}}_{1*}^\dagger, \hat{p}_{1*}^\dagger)^\mathrm{T}$, needed to enforce the compatibility condition. The reader interested in more details is referred to Sipp and Lebedev (2007) and Meliga and Chomaz (2011) where an exhaustive description can be found along with details on the numerical techniques employed to solve the various linear and nonlinear problems arising at each order in ϵ. The interest of the approach is threefold:

- the flow dynamics reduces to a single degree of freedom being the complex amplitude $\mathcal{A}$ along the bifurcating eigenmode direction, so that the governing equations can be time-marched by means of standard Runge–Kutta or Adams–Bashforth time-marching schemes,
- since the cylinder displacement is only of order ϵ^3, the flow problem is that of the wake past a fixed cylinder, up to the second order ϵ^2. The coupling results from the application of the compatibility condition, so that no specific treatment is required in the numerics to take into account the motion of the cylinder boundary,
- the coefficients λ, μ, α, β in (2) can be expressed analytically as scalar products between the adjoint eigenmode and appropriate terms built from the low-order solutions $\boldsymbol{q_i}$ ($0 \le i \le 2$), their numerical value being taken from Meliga and Chomaz (2011) as

$$\lambda = 9.153 + 3.239\mathrm{i}, \quad \mu = 308.9 - 1025\mathrm{i}, \quad \alpha = 0.03492 + 0.01472\mathrm{i}, \quad \beta = 1. \tag{6}$$

Since we aim at exploiting the vortex-induced vibrations of a cylinder in water streams, the model must be used with mass ratios departing from the fourth-order scaling. Consequently we use the extended model derived in Meliga and

Chomaz (2011) for low mass ratios and mass-damping parameters. The latter relies on a modified structure equation in which the retained lift force of order ϵ^5 is complemented by the contributions of added mass and added damping coming at order ϵ^7 in the expansion (Blevins, 1990; Govardhan and Williamson, 2000). These terms can be legitimately neglected when using the balance defined above, meaning that the original model is exact in the range of parameters for which it has been derived rigorously. Only in the limit of low mass ratios and low mass-damping do the corrective terms acquire significance. Namely, they put an upper bound on the effective mass and damping, which results in an appropriate self-limiting structural response. This extension results in little modification of the governing equations, as discussed in the original article. Consequently, the evolution operator is from now on renamed $\check{\mathbf{M}}$, but we keep discussing the main features of the model using systems (2–3).

2.2. Main results

The ability of the model to reproduce the physics of VIVs has been assessed from the study of the nonlinear limit cycles, i.e. the periodic, synchronized orbits reached by the system at large time whose analytical expressions have been derived in Meliga and Chomaz (2011). They can be sought as the equilibrium points of system (3), satisfying

$$\check{\mathbf{M}}(\mathbf{Q}_\infty) = \mathbf{0},\tag{7}$$

where all related quantities are from now on denoted by the subscript ∞. The simultaneous existence of multiple limit cycles is responsible for the onset of a complex hysteretic behavior in the lock-in regime. In practice, there exist always either one or three limit cycles, as a result of the synchronized phase-shift Eq. (3c) reducing to a third-order polynomial equation in $\tan\phi$ admitting either one or three real roots. We present in Fig. 2(a) the limit cycle amplitude of the cylinder displacement $|\mathcal{Y}_\infty|$ as a function of the cylinder natural frequency ω_s, for a Reynolds number Re=50 and a structural damping $\gamma = 0.01$. Two mass ratios are considered, namely $m=10\,000$ (i.e. approximately steel in air, shown as the gray line), for which there exist a single limit cycle, and $m=200$ (black line), for which there exist up to three limit cycles over specific ranges of frequencies. For clarity, we denote by *upper* cycle the limit cycle yielding the largest displacement amplitude, as shown by the thick lines in Fig. 2(a), and by *lower* cycle the limit cycle yielding the smallest displacement amplitude.

The limit cycles can also be used to gain insight into the energy extraction problem. Since all solutions are periodic on a given cycle, the mean mechanical energy averaged over a period is zero, and the mean work received from the fluctuating lift force is entirely dissipated by structural damping. Meliga and Chomaz (2011) have shown that at leading-order, the mean dissipated energy is a simple function of the displacement amplitude

$$\mathcal{E}_\infty = 2\omega_s\gamma \frac{1}{T_\infty} \int_0^{T_\infty} \left(\frac{\mathrm{d}y_s}{\mathrm{d}t}\right)^2 \mathrm{d}t = 4\omega_s\omega_*^2\gamma|\mathcal{Y}_\infty|^2,\tag{8}$$

since the time-derivative is replaced by the factor $i\omega_*$ in the present expansion. It can be inferred from (8) that there must exist an optimal parameter setting for which the dissipated energy is maximum. On the one hand, the flow-cylinder system must be synchronized for the cylinder displacement amplitude to be large, meaning in particular that the upper limit cycle is the only one of practical interest. On the other hand, the energy tends to zero in the limit $\gamma \gg 1$ where the work received from the lift force is limited by the low amplitude of the displacement, and in the limit $\gamma \ll 1$ where the displacement is self-limited. As an
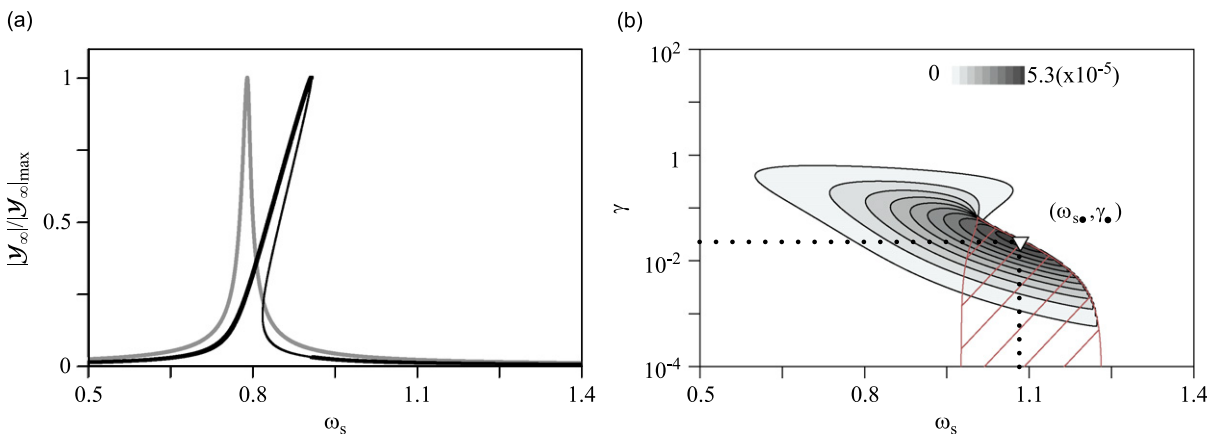
Fig. 2. (a) Amplitude of the cylinder displacement $|\mathcal{Y}_\infty|$ computed on the limit cycle as a function of the natural frequency ω_s for $m=10\,000$ (gray line) and $m=200$ (black line). The amplitude on each curve is normalized by its maximum value to facilitate the reading, and the upper cycle yielding the maximum displacement amplitude is enhanced by the thick lines—Re=50, $\gamma = 0.01$. (b) Energy $\mathcal{E}_\infty$ dissipated by structural damping on the upper limit cycle: isocontours in the (ω_s,γ)-plane. The system is hysteretic for parameter couples located within the red striped area, and the position of the global maximum is indicated by the inverted triangle—Re=50, $m=10$.

illustration, we present in Fig. 2(b) isocontours of the dissipated energy $\mathcal{E}_\infty$ for a Reynolds number Re=50 and a mass ratio $m=10$ corresponding approximately to steel in water. This map has been obtained from $\sim 10^6$ computations carried out in the (ω_s, γ)-plane, only the upper cycle being taken into account. This yields a discontinuity shown as the thin red line, corresponding to parameter settings where the system undergoes a transition from a hysteretic to a non-hysteretic regime (the hysteresis zone being indicated by the oblique stripes). These results also demonstrate the existence of a specific pair $(\omega_{s\bullet}, \gamma_\bullet)$ indicated by the inverted triangle, for which the dissipated energy reaches a global maximum $\mathcal{E}_{\infty\bullet}$. For the mass ratio and Reynolds numbers considered, we obtain $\omega_{s\bullet}=1.08$ and $\gamma_\bullet=0.023$. This set of parameter arises naturally from an exhaustive investigation in the structural parameter space, and defines the "tuning" which optimizes the magnitude of energy harvested from the free stream by an energy production device. Note that it lies at the edge of the discontinuity line. This may have important consequences for the application, since small inaccuracies in the structural parameters may tip the system outside the hysteresis zone, hence resulting in a dramatic drop of the harnessed energy.

2.3. Integration of feedback control in the model

We propose now to assess the ability of flow control techniques to improve both the robustness of the optimal tuning and the amount of dissipated energy at disposal to be harvested. To this end, we assume that a localized blowing and suction velocity $\boldsymbol{u_c}$ is imposed by an actuator positioned on the cylinder wall. We use a three-degree of freedom actuation for which the position, incidence and magnitude of the control velocity can be set independently, as sketched in the lower part of Fig. 3. The control velocity is written as

$$\boldsymbol{u}_c = u_c(t)\delta(\theta-\theta_c)(\sin\vartheta\boldsymbol{t}+\cos\vartheta\boldsymbol{n}), \tag{9}$$

where u_c is the time-dependent velocity amplitude, θ is the azimuthal position along the cylinder wall whose origin is taken at the rear stagnation point, $\delta(\theta)$ is a Dirac distribution, θ_c indicates the position where the control is applied, $\boldsymbol{t}$ and $\boldsymbol{n}$ are the wall-tangent and wall-normal vectors, and ϑ is the angle of incidence of the control velocity with respect to the tangent vector ($\vartheta=\pm\pi/2$ for a wall-normal velocity).

We assume that the growth of the flow disturbances is forced at order ϵ by a velocity of order ϵ^3 applied near-resonance, and define a new complex amplitude U_c evolving on the slow time

$$u_c = \epsilon^3 U_c(T)e^{i\omega_* t} + \text{c.c.} \tag{10}$$

The integration of the control in the model results from the application of a modified compatibility condition, yielding an additional term in the flow equation

$$\frac{\mathrm{d}\mathcal{A}}{\mathrm{d}t} = \lambda\left(\frac{1}{\text{Re}_*}-\frac{1}{\text{Re}}\right)\mathcal{A}-\mu\mathcal{A}|\mathcal{A}|^2+\alpha\mathcal{Y}+\eta, \tag{11}$$

but leaves the structure equation unchanged. Applying the results of Meliga and Chomaz (2011) to the velocity distribution (9), we obtain a simple expression for the η coefficient:

$$\eta = \chi\mathcal{U}_c, \quad \text{with } \mathcal{U}_c=\epsilon^3 U_c. \tag{12}$$

The control velocity, therefore, shows up explicitly in the equation, χ being a receptivity coefficient defined from the conveniently normalized adjoint eigenmode as

$$2\chi = \hat{p}_{1*}^\dagger\sin\vartheta+\frac{1}{\text{Re}_*}\sin\vartheta(\boldsymbol{\nabla}\hat{\boldsymbol{u}}_{1*}^\dagger\cdot\boldsymbol{n})\cdot\boldsymbol{n}+\frac{1}{\text{Re}_*}\cos\vartheta(\boldsymbol{\nabla}\hat{\boldsymbol{u}}_{1*}^\dagger\cdot\boldsymbol{n})\cdot\boldsymbol{t}, \tag{13}$$

with all adjoint quantities evaluated at the actuator position θ_c.
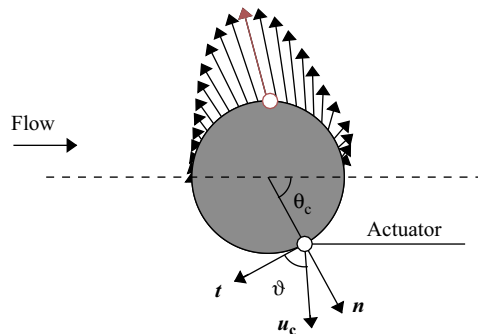
Fig. 3. Schematic of the control actuation: an actuator located at the position θ_c produces a velocity of amplitude u_c with an angle ϑ with respect to the tangent vector. The azimuthal distribution of maximum receptivity it plotted at the wall of the upper half-cylinder. The orientation of the arrows indicates the optimal incidence selected at the corresponding actuator position. The actuator used in Sections 3–5 is marked by the red circle symbol.

The chosen approach is that of proportional feedback control. We assume that the state of the system is accessed through measurements of the cylinder position, and that the actuator applies the control velocity with a certain gain k and phase shift φ. Since the measured displacement is of order ϵ^3, this requires to use a gain of order unity for the control velocity to be of order ϵ^3. The complex amplitude $\mathcal{U}_c$ is then simply related to the displacement amplitude by

$$\mathcal{U}_c = k\,e^{i\varphi}\mathcal{Y} = \kappa\mathcal{Y}, \quad \text{with } \kappa = ke^{i\varphi}, \tag{14}$$

so that the η coefficient ultimately reads

$$\eta = \chi\kappa\mathcal{Y}. \tag{15}$$

Owing to the specific form of the η control coefficient, the forced evolution equations can be written in compact form as

$$\frac{d\mathbf{Q}}{dt} = \check{\mathbf{M}}(\mathbf{Q},\kappa), \tag{16}$$

where the forced evolution operator is deduced in a straightforward manner from its unforced counterpart by the transformation

$$\alpha \longrightarrow \alpha + \chi\kappa. \tag{17}$$

This means that the results pertaining to the unforced system carry over, including the existence of limit cycles and the analytical relation (8) providing the mean energy dissipated by damping. The same formalism holds in case the structural motion is accessed via different types of measurements, for instance the cylinder velocity or acceleration. Since the time-derivative is replaced by the factor $i\omega_*$, relation (15) remains invariant provided the complex gain is redefined as

$$\kappa = i\omega_* ke^{i\varphi} \quad \text{(velocity)}, \quad \kappa = -\omega_*^2 ke^{i\varphi} \text{ (acceleration)}. \tag{18}$$

3. Optimization of the limit cycle orbit

We undertake first the control of the limit cycle orbit. The point of the analysis is to determine the value of the complex gain, denoted by κ_∞ for consistency, which maximizes the energy gain

$$\mathcal{G}_\infty(\kappa_\infty) = \mathcal{E}_\infty(\kappa_\infty) - \mathcal{C}_\infty(\kappa_\infty), \tag{19}$$

where $\mathcal{C}_\infty$ is the cost of the control defined here as the mean kinetic energy expended by the actuator over a limit cycle period, i.e.

$$\mathcal{C}_\infty = \frac{1}{T_\infty}\int_0^{T_\infty}\frac{1}{2}u_c^2\,dt = |\mathcal{U}_c|^2 = |\kappa_\infty|^2|\mathcal{Y}_\infty|^2, \tag{20}$$

at leading-order.

3.1. Choice of the actuation parameters

At this stage, there remain four real unknowns to be determined, namely the position of the actuator θ_c, the incidence of the control velocity ϑ, and the amplitude and phase of the complex feedback gain κ_∞. It can be anticipated that θ_c and ϑ must be chosen for the magnitude of the receptivity coefficient $|\chi|$ to be maximum, since it follows from relations (15)–(20) that the orbit of the forced cycles depends only on the product $\chi\kappa_\infty$ while the cost of the control depends only on the norm $|\kappa_\infty|$. Maximum receptivity yields minimum cost, and thereby, maximum gain.

Since all results are invariant under the reflection $\theta_c \rightarrow -\theta_c$, we restrict the search for the actuator position to the range $\theta_c \in [0;\pi]$. The azimuthal distribution of maximum receptivity at the cylinder wall is sketched in the upper part of Fig. 3, where the orientation of a vector arrow indicates the incidence of the control velocity selected at the corresponding actuator position. The magnitude of the receptivity coefficient reaches a maximum for the position $\theta_c = 1.54$ ($\sim 88°$) shown as the red circle, where $\chi = -0.0674 - 0.0173i$. The corresponding angle of incidence is $\vartheta = 1.85$ ($\sim 106°$), i.e. the control velocity is almost normal to the cylinder wall. This is consistent with the results of Giannetti and Luchini (2007), who showed that the level of receptivity to a wall-normal velocity is maximum in the vicinity of the separation points.

3.2. Adjoint-based optimization algorithm

In order to determine the feedback gain κ_∞, we use the framework of Lagrangian constrained optimization, which requires the definition of the following ingredients:

- state variables, i.e. the limit cycle quantities $\mathbf{Q}_\infty$,
- design variables to be optimized, i.e. the complex gain κ_∞,
- state equations defining the constraint to be satisfied, i.e. the synchronized, forced limit cycle equations

$$\check{\mathbf{M}}(\mathbf{Q}_\infty\kappa_\infty) = \mathbf{0}, \tag{21}$$
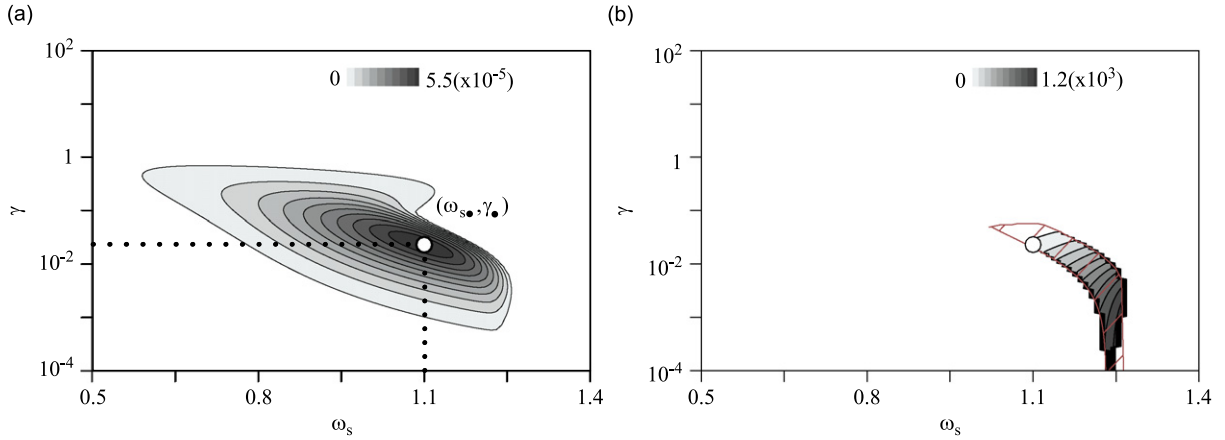
Fig. 4. (a) Isocontours of the energy gain $\mathcal{G}_\infty$ computed as a function of the natural frequency ω_s and the structural damping γ. The position of the global maximum is indicated by the circle—Re=50, m=10. (b) Same as (a) for the effectiveness coefficient ς defined in (22) and quantifying the net effect of the control. In the striped area, the system is non-hysteretic in the absence of control, but hysteretic if forced with the optimal feedback control.

- a cost functional chosen as $\mathcal{J} = -\mathcal{G}_\infty$, the minus sign ensuring that the optimal gain corresponds to a minimum of the functional, so that all classical methods developed for minimization problems apply.[1]

This problem is solved via an adjoint-based conjugate gradient algorithm presented in Appendix A. At each iteration, the cost functional is evaluated along the descent direction. In case the system is hysteretic, three such cost functionals are computed, and only the limit cycle yielding the minimum value is retained, which turns out to be systematically the upper cycle (this result being not obvious a priori, albeit intuitively expected).

Since we investigate a two-degree of freedom optimization problem, the minimum of the cost functional can also be determined by a graphical method. In practice, the time needed to determine a specific optimum with reasonable accuracy renders this approach unsuitable if minimization problems are to be solved in massive numbers, as is the case in the present analysis. Moreover, the adjoint framework can be easily extended to encompass more complex control strategies involving multiple actuators and large control parameter spaces. Nevertheless, we have compared the results of both methods for various parameter settings and have checked a posteriori that the optimum returned by the adjoint-based algorithm is a global minimum, which cannot be guaranteed by the theory since the state equations are nonlinear.

3.3. Results

From now on, we set the Reynolds number and mass ratios to Re=50 and m=10. The results of the optimization procedure are illustrated in Fig. 4(a), where we present isocontours of the optimal energy gain. This map has been built from the resolution of ~ 2500 optimization problems in the (ω_s, γ)-plane, each of which ended in the computation of a specific optimal feedback gain. Since all energy gains are positive, the optimized energy at disposal to be harvested is systematically larger than the cost expended by the actuator. These results also demonstrate the existence of a global maximum $\mathcal{G}_{\infty \bullet}$ reached for $\omega_{s \bullet} = 1.10$ and $\gamma_\bullet = 0.023$, for which the optimal feedback gain is such that $|\kappa_{\infty \bullet}| = 0.0408$ and $\arg \kappa_{\infty \bullet} = -0.164$.

The same results are presented in Fig. 4(b) in terms of the effectiveness coefficient

$$\varsigma = \frac{\mathcal{G}_\infty - \mathcal{E}_\infty|_{\kappa = 0}}{\mathcal{E}_\infty|_{\kappa = 0}}, \tag{22}$$

quantifying the net effect of the control. All values are positive, meaning that the unforced system is never optimal. Note the existence of two discontinuities marked by the thin red lines, that have been checked to correspond to the parameter settings where the unforced and forced systems, respectively, undergo the transition from hysteretic to non-hysteretic behavior. The intermediate striped region, where the system is non-hysteretic in the absence of control but hysteretic when the optimal control is applied, can be seen to match remarkably well the region of large effectiveness, meaning that the main effect of the optimal control is to widen the range of structural parameters producing hysteresis.

---

[1] In the general framework of constrained optimization, one needs to specify the value of a weighting parameter denoted l^2. The latter does not bear any physical significance but simply penalizes the control cost with respect to the objective: if chosen large, then the control is "expensive", if chosen small, then the control is "cheap". From this point of view, the cost functional should read here $\mathcal{J} = -\mathcal{E}_\infty + l^2 \mathcal{C}_\infty$. Nevertheless, the need for this weighting coefficient relies on the fact that the cost functional often combines dimensionally inhomogeneous physical quantities, for instance a force and an energy in case one is interested in drag reduction problems. This restriction does not apply here where the energy gained and the energy spent must have the same weight, which is equivalent to set $l^2 = 1$.

(a) (b)
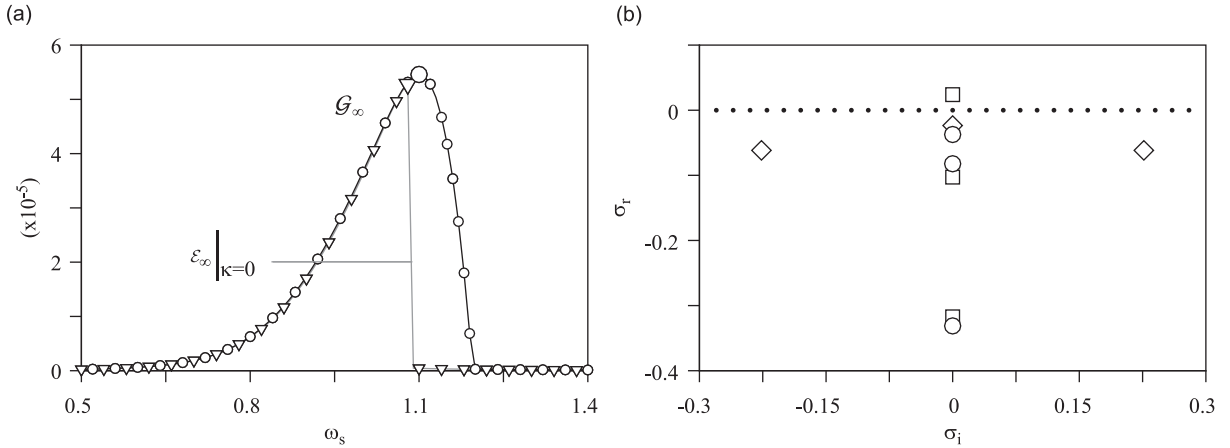
Fig. 5. (a) Magnitude of the energy gain as a function of the natural frequency ω_s. The black line with circles (resp. the gray line with inverted triangles) pertains to the forced system (resp. the unforced system), and the large symbols indicate the position of the global maxima—Re=50, m=10, $\gamma=\gamma_\bullet$. (b) Eigenvalue spectra of the limit cycles forced by the asymptotic optimal control designed in Section 3. The circle, diamond and square symbols refer to the upper, lower and intermediate cycle, respectively—Re=50, m=10, $\omega_s = \omega_{s\bullet}$, $\gamma=\gamma_\bullet$, $\kappa=\kappa_{\infty\bullet}$.

Note that the global maximum lies in a zone of moderate effectiveness with $\varsigma \sim 3.5\%$, as a result of the unforced system being already hysteretic. Nevertheless, the control induces a significant difference in the relative position of the global maximum: the latter lies no longer at the edge of the transition line, but in a broadened area where the gain exhibits smooth variations, as depicted in Fig. 5(a) where we present the energy available from the flow, as extracted from Figs. 2(b) and 4(a) along the horizontal line $\gamma=\gamma_\bullet$ (the black line with circles pertains to the forced case, and the gray line with inverted triangles pertains to the unforced case). One sees that the control renders the system more robust, in the sense that it remains hysteretic even though small discrepancies in the structural parameters may exist. As an example, if the natural frequency is larger than its optimal value by only 2%, the magnitude of energy harnessed from the forced system decreases by only 4%, but that harnessed from the unforced system drops by almost 100%, hence resulting in a tremendous effectiveness $\varsigma \sim 500\%$.

4. A transient phase-shift algorithm to force the large time dynamics

From now on, we set $\omega_s = \omega_{s\bullet}$, $\gamma=\gamma_\bullet$ and $\kappa_\infty = \kappa_{\infty\bullet}$, i.e. the system is forced by the optimal feedback control determined in Section 3, referred to as the *asymptotic* optimal feedback control. We investigate the transient dynamics, where the flow and cylinder amplitudes are no more periodic, nor synchronized. Consequently, we adopt a convenient, instantaneous description for all quantities of interest, including the energy gain $\mathcal{G}$ whose leading contribution is split into

$$\mathcal{G}(t) = \mathcal{G}_t(t) + \mathcal{G}_0(t), \tag{23}$$

with

$$\mathcal{G}_t = -(2\omega_s\omega_*^2\gamma + \tfrac{1}{2}\kappa_{\infty\bullet}^2)\mathcal{Y}^2 e^{2i\omega_* t} + \text{c.c.}, \tag{24a}$$

$$\mathcal{G}_0 = 4\omega_s\omega_*^2\gamma|\mathcal{Y}|^2 - |\kappa_{\infty\bullet}|^2|\mathcal{Y}|^2. \tag{24b}$$

When the system reaches a limit cycle, the contribution arising from (24a) vanishes when averaging over a cycle period, whereas that arising from (24b) yields the value of the optimal gain $\mathcal{G}_{\infty\bullet}$ reported in Section 3.

Taking into account the transient dynamics adds significant complexity to the problem. Several points need to be addressed, including

- *is the optimal upper limit cycle stable to external disturbances*?
- *since the system is hysteretic, does there exist any other stable cycle*?
- *if so, is there a risk for the system to drop from the upper cycle, albeit stable*?

4.1. Stability of the forced limit cycles

Small-amplitude disturbances to the limit cycle growing exponentially in time satisfy the eigenvalue problem

$$\sigma\boldsymbol{Q} + \check{\boldsymbol{L}}(\boldsymbol{Q}_\infty, \kappa)\boldsymbol{Q} = \boldsymbol{0}, \tag{25}$$

where $\check{\boldsymbol{L}} = \partial\check{\boldsymbol{M}}/\partial\boldsymbol{Q}$ is the linearized evolution operator. When the evolution equations are used in their recast form, the latter operator can be written as a 3×3 matrix whose complete expression is provided in Appendix A, and the stability
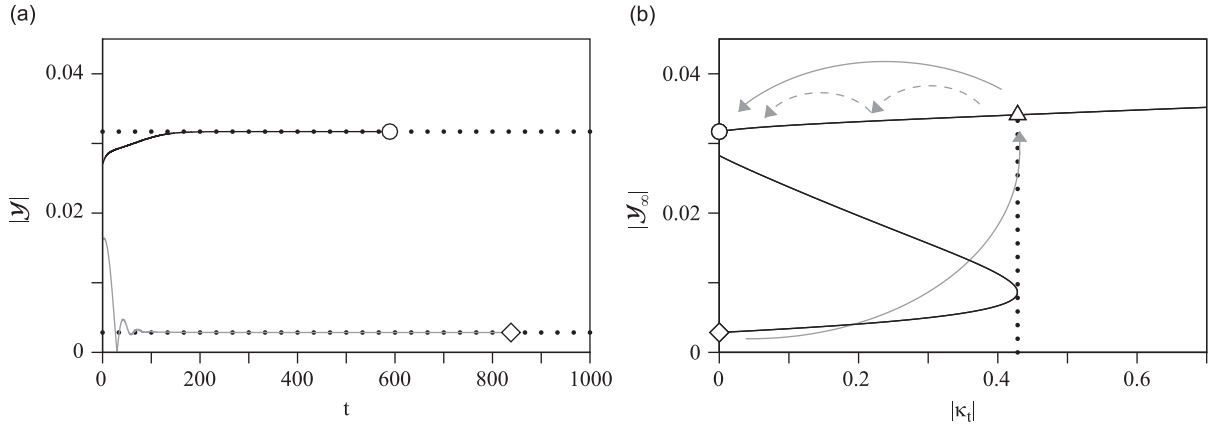
Fig. 6. (a) Time-evolution of the cylinder displacement amplitude when the system is forced only by the asymptotic optimal control. The black and gray lines correspond to two independent simulations initialized with random initial conditions, whereas the circle and diamond indicate the upper and lower limit cycle amplitudes reached at large time. (b) Phase-shift control algorithm: the solid line depicts the displacement amplitude computed on the limit cycle as a function of the transient gain amplitude $|\kappa_t|$, the phase being set to $\arg\kappa_t = -0.995$. The gray shaded area indicates the range of amplitudes allowing to suppress hysteresis. The triangle marks the backup limit cycle for the amplitude $|\kappa_t| = 0.428$ used in the numerics. The upper and lower cycles shown in (a) to be reached if no transient control is applied are also shown in (b) as the circle and diamond on the $|\kappa_t| = 0$ axis. For both plots, Re $=50$, $m=10$, $\omega_s = \omega_{s\bullet}$, $\gamma = \gamma_\bullet$, $\kappa_\infty = \kappa_{\infty\bullet}$.

analysis reduces to the computation of three eigenvalues. The spectra of the forced cycles are indicated by the various symbols in Fig. 5(b). We find that the upper cycle (circles) and the lower cycle (diamonds) are stable since all three eigenvalues have negative real parts. In contrast, the intermediate cycle (squares) is unstable.

Confirmation comes from the time-marching of the governing equations using a fourth-order Runge–Kutta scheme. When the upper cycle quantities are perturbed by randomly generated disturbances of small but prescribed magnitude, we find that the system always returns to its original orbit (not shown here). This is no longer true when the amplitude of the perturbation reaches moderate magnitudes. As an illustration, we present in Fig. 6(a) the displacement amplitude $|\mathcal{Y}|$ as a function of time for two independent simulations. In both cases, the magnitude of the initial disturbance represents 50% of the limit cycle amplitude, and the time-integration is carried out until the relative variation of the cylinder amplitude becomes less than a threshold value set here to 10^{-12}. In the first simulation, shown as the black line, the system converges smoothly to the upper cycle, as indicated by the upper horizontal dotted line. In the second one, shown as the gray line, the system exhibits a more complex transient behavior and finally converges to the lower cycle.

4.2. Phase-shift control

Since we aim at exploiting VIVs for energy production, the previous results underline the importance of designing a specific control aiming at enforcing a systematic convergence to the upper cycle. To this end, we assume that the complex gain can depart from its asymptotic optimal value in finite time, according to

$$\kappa = \kappa_t(t) + \kappa_{\infty\bullet}, \quad \text{with} \lim_{t \to \infty} \kappa_t(t) = 0, \tag{26}$$

where κ_t is a transient gain meant to introduce an artificial detuning between both oscillators. This so-called phase-shift control is expected to enforce the existence of a single limit cycle since Meliga and Chomaz (2011) reported a close correlation between the onset of hysteresis and the cylinder displacement being in phase with the unsteady lift fluctuations.

In practice, we use a piecewise constant transient gain, whose value is non-zero only over a single and finite time interval. The principle of the phase-shift control is depicted in Fig. 6(b), where we present the limit cycle displacement amplitude computed as a function of the gain amplitude $|\kappa_t|$, the phase being $\arg\kappa_t = -0.995$, as will be explained in the following. The forced limit cycles previously reached in the absence of transient control are retrieved as the circle and diamond symbols on the $|\kappa_t| = 0$ axis. It turns out that the system can be rendered non-hysteretic by setting the amplitude to any value in the range $|\kappa_t| > 0.428$, hence yielding the following algorithm:

- the phase-shift control is initially off ($\kappa_t = 0$), and remains off as long as the system evolves on the upper cycle,
- if at some point, the system is found to evolve on the lower cycle (this information being available from the measurements of the cylinder motion), then the phase-shift control is switched on. Using an appropriate transient gain $\kappa_t \neq 0$ which suppresses hysteresis, the system is forced to converge towards a prescribed cycle referred to as the backup cycle (triangle symbol/lower gray solid arrow in Fig. 6(b)),
- once convergence is identified, the phase-shift control is switched off, the oscillators are put back into phase, and the system converges towards the upper cycle (upper gray solid arrow).

(a)

(b)
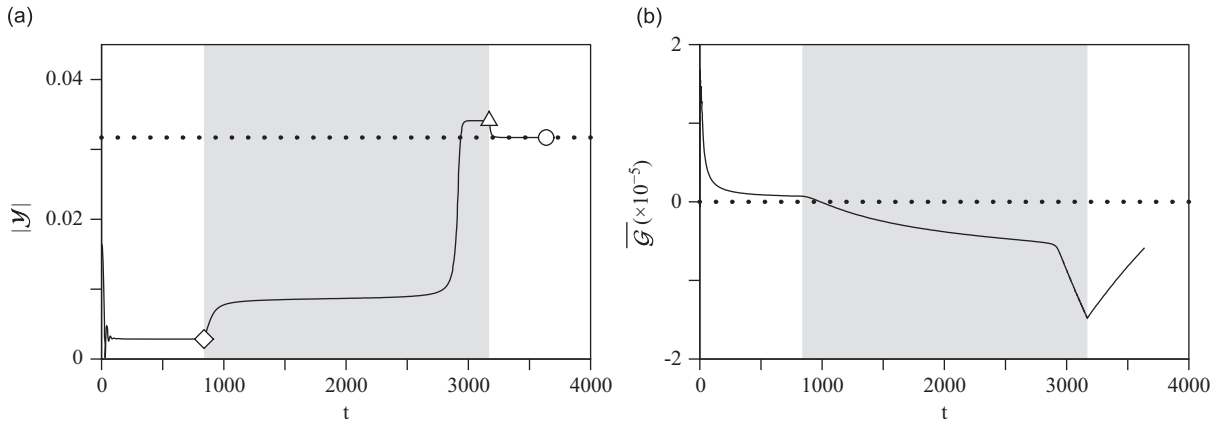
Fig. 7. (a) Time-evolution of the cylinder amplitude when the system is forced by both the phase-shift control *and* the asymptotic optimal control. The gray shaded area corresponds to the time interval over which the phase-shift control is applied—Re = 50, $m = 10$, $\omega_s = \omega_{s\bullet}$, $\gamma = \gamma_\bullet$ and $\kappa_\infty = \kappa_{\infty\bullet}$. (b) Same as (a) for the integrated gain defined by (28).

In practice, choosing the value of the complex gain is a two-step procedure. First, we prescribe the phase and determine the amplitude minimizing the kinetic energy asymptotically expended by the actuator to maintain the system on the backup cycle, i.e.

$$\mathcal{C}_t = |\kappa_t|^2 |\mathcal{Y}_\infty|^2. \tag{27}$$

Second, we vary the phase and repeat the first step. The key idea of the control lies in the fact that the path back from the backup to the upper cycle must be *continuous* for the system to end up systematically on the upper cycle. Consequently, we exclude all amplitudes allowing to suppress hysteresis but yielding a *discontinuous* path. We ultimately retain the phase and associated amplitude for which the kinetic energy reaches a global minimum. We obtain here $|\kappa_t| = 0.428$ and $\arg\kappa_t = -0.995$, the associated backup cycle being precisely the one indicated by the triangle symbol in Fig. 6(b).

This algorithm can be easily implemented in the time-marching procedure. We present in Fig. 7(a) the time-evolution of the displacement amplitude, this simulation having been initialized with the condition shown in Section 4.1 to bring the system to the lower cycle in case no transient control is used. The phase-shift control is applied at $t \sim 830$ (gray shaded area), immediately after convergence on the lower cycle has been identified from the measurements. A complex transient behavior develops before the system reaches the backup cycle at $t \sim 3200$ (triangle symbol). At this stage, the phase-shift control is switched off, a new transient can be observed but the system finally reaches the upper cycle at $t \sim 3600$ (circle symbol). This result is actually general for any initial condition bringing the system to the lower cycle, since the phase-shift control is switched on only once the system has reached the lower cycle, hence illustrating the robustness of the method. Would the distance between the backup and upper cycles have been too large to ensure a systematic convergence, then the approach could have been easily extended to include secondary backup cycles. The resulting algorithm would have then consisted in gradually decreasing the value of the transient gain, and in jumping from one limit cycle to another in Fig. 6(b), as indicated by the dashed arrows.

In order to gain insight into the energy production problem, we have also monitored the time-evolution of the integrated gain defined as

$$\overline{\mathcal{G}}(t) = \frac{1}{t} \int_0^t \mathcal{G}(\tau) d\tau, \tag{28}$$

and counting the additional cost of the phase-shift control, which is achieved by replacing $\kappa_{\infty\bullet}$ by $\kappa_t + \kappa_{\infty\bullet}$ in (24). Results are presented in Fig. 7(b), where it can be seen that the initial convergence to the lower cycle results in a decrease of the gain. Note the change in slope at $t \sim 900$, i.e. slightly after the phase-shift control has been switched on. Additional energy is now expended by the actuator to force the return onto the upper cycle, so that the gain keeps decreasing over a large time interval. Only when the phase-shift control is switched off does the gain start increasing, but the value achieved by the time the system finally returns to the upper cycle is still negative. These results suggest that energy may be extracted only when the system evolves on the upper cycle. In contrast, in case the system quits its orbit after having encountered external disturbances, a fraction of this energy must be spent to feed the phase-shift control.

5. Measuring the flow motion: an alternative strategy

We propose now to use an alternative feedback strategy designed from measurements of the flow motion (Case 2), hence departing from the previous strategy designed from measurements of the cylinder motion (Case 1). We use the

same actuator as for Case 1 whose setup has been guided by receptivity arguments, independently of the technique used to design the feedback loop. We assume now that a sensor measures an appropriate fluctuating flow quantity, the procedure being exemplified by considering a pressure probe located on the cylinder wall at the azimuthal position θ_p. When expanding the measured signal denoted by $p'(t)$ in series of ϵ, we find that the leading-order contribution is simply proportional to the pressure component of the bifurcating eigenmode of order ϵ, i.e.

$$p'(t,x_p,y_p) = \epsilon A(T)\hat{p}_{1*}(\theta_p)e^{i\omega_* t} + \text{c.c.} \tag{29}$$

For the control to be effective at order ϵ^3, we must now use a gain of order ϵ^2, which yields the velocity amplitude $\mathcal{U}_c$ in the form

$$\mathcal{U}_c = ke^{i\varphi}\hat{p}_{1*}(\theta_p)\mathcal{A}. \tag{30}$$

In result, the η coefficient as defined from (12) is now a function of the flow disturbance amplitude, and reads

$$\eta = \chi\kappa\mathcal{A}, \quad \text{with } \kappa = ke^{i\varphi}\hat{p}_{1*}(\theta_p). \tag{31}$$

The asymptotic feedback gain κ_∞ can be determined using the adjoint-based approach presented in Section 3, the existence of such forced cycles being still guaranteed since the forced evolution operator is obtained from its unforced counterpart by the transformation

$$\lambda \to \lambda + \chi\kappa_\infty. \tag{32}$$

One must only pay attention to the fact that the cylinder amplitude is replaced by the flow amplitude in the cost definition (20), which induces some modifications in the algorithm. However, it can be anticipated (and it has been indeed checked with the numerics) that the results follow in a straightforward manner from those obtained in Case 1 according to

$$\kappa_\infty|_{\text{Case 2}} = \frac{\mathcal{y}_\infty}{\mathcal{A}_\infty}\kappa_\infty|_{\text{Case 1}}, \tag{33}$$

so that the optimal gain yielding the global maximum in Case 2 is now $|\kappa_{\infty\bullet}| = 0.0771$ and $\arg\kappa_{\infty\bullet} = -0.253$. When the system is forced by the corresponding asymptotic optimal law, its stability properties are reminiscent of those documented in Section 4.1 for Case 1, namely the upper and lower cycles are stable, and the intermediate cycle is unstable, with only minor discrepancies in the eigenvalue spectra (not shown here). Consequently, the main conclusion to be drawn is that it is rigorously equivalent to optimize the orbit of the limit cycle with either method.

This is no longer true when the transient dynamics is taken into account. We have repeated the design procedure of the phase-shift algorithm, and have obtained a new value for the transient gain, namely $|\kappa_t| = 0.337$ and $\arg\kappa_t = 0.0698$. We present in Fig. 8(a) the time-evolution of the displacement amplitude obtained by time-marching the resulting evolution equations, this simulation having been initialized with the condition shown in Section 4.1 to bring the system to the lower cycle in the absence of transient control, and used in Section 4.2 to assess the efficiency of the phase-shift algorithm. The new results pertaining to Case 2 are shown as the red line, while the results pertaining to Case 1 are reported for comparison as the black line. It is striking that the phase-shift algorithm acts much more rapidly when using flow measurements. Indeed, the time interval during which the control is applied is reduced here by more than 50%, which may come from different stability features of the underlying backup cycles or from different levels of non-normality of the forced system (Chomaz, 2005). This induces a significant reduction in the cost of the control. As a result, the integrated gain shown in Fig. 8(b) returns to positive values even though the system has not yet reached the backup cycle, which
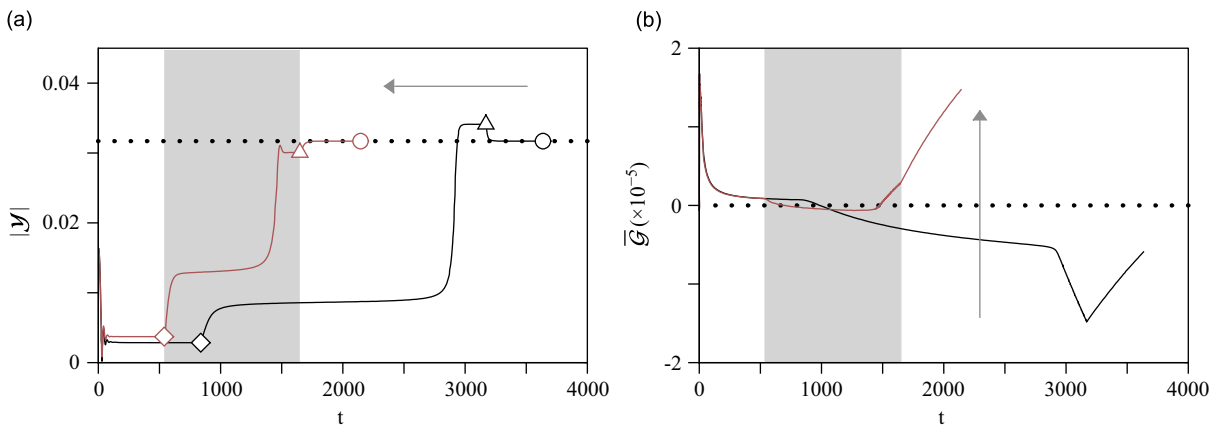
Fig. 8. (a) Time-evolution of the cylinder amplitude when the system is forced by both the phase-shift control *and* the asymptotic optimal control. The red and black curves correspond to Case 2 and Case 1, respectively, both simulations being initialized with the same initial condition—Re=50, m=10, $\omega_s = \omega_{s\bullet}$, $\gamma = \gamma_\bullet$ and $\kappa = \kappa_{\infty\bullet}$. (b) Same as (a) for the integrated gain.

yields a positive value by the time the system has finally returned to the upper cycle. These results suggest that energy can now be harnessed not only when the system evolves on the upper cycle, but also when transient control is required. Again, this result is general to any initial condition bringing the system down to the lower cycle, hence singling out feedback control from flow measurements as a promising strategy in the perspective of energy production.

6. Concluding remarks

In this study, we consider the ability of flow control to optimize the magnitude of energy dissipated by a spring-mounted, circular cylinder at low Reynolds numbers, which is of practical interest if VIVs are to be used for energy production. The dynamics of the forced flow-cylinder system is described using an analytical model derived by an asymptotic analysis of the Navier–Stokes equations, forced by the cylinder displacement and by a proportional feedback control with actuation by an unsteady jet at the cylinder wall. The main advantage of this approach is that the model depends explicitly on the control velocity, which eases considerably the choice of convenient actuation parameters from physically motivated receptivity arguments.

We use first an adjoint-based algorithm to optimize the energy gain, i.e. the difference between the mean energy harvested at large time from the limit cycle and the mean kinetic energy expended for control purposes. A parametric study is undertaken which shows that there exist specific structural parameters for which the energy gain is maximum, hence defining the precise conditions at which the system should be operated. This optimum represents an increase in the harvested energy by 3.5% with respect to the unforced case. More importantly, the control also results in a significant improvement of the system robustness with respect to small inaccuracies of the structural parameters. Owing to the existence of multiple stable limit cycles, a phase-shift transient control algorithm is introduced to force the convergence of the system to the limit cycle yielding the largest magnitude of harnessed energy. The efficiency of this technique is compared for two feedback approaches using distinct types of measurements. We find significant differences in the time needed to enforce convergence to the optimal cycle, which results in energy being spent when feedback is designed from cylinder measurements, and in energy being harnessed when feedback is designed from flow measurements.

In conclusion, it is worth noticing that this asymptotic formalism can be generalized to encompass the effect of a second-order stationary blowing or suction control velocity, a highly attractive approach owing to the simplicity of its practical implementation. This yields a nonlinear model almost identical to that used in the present study, the main difference being that the receptivity coefficient used to choose the actuation parameters relies on the computation of a so-called adjoint base flow, i.e. an additional flow solution characterizing the effect of a small-amplitude stationary control on the linear growth rate of an instability mode (Hill, 1992). Nevertheless, it can be inferred (and it has been checked from preliminary computations) that the cost is higher than in the case of feedback control, since the control velocity is larger by one order of magnitude. This results in poor efficiency, hence making feedback control designed from flow measurements the most promising approach for an application to the energy harvesting problem.

Appendix A. The static optimization algorithm

This appendix is devoted to the presentation of the algorithm used in Section 3 to determine the optimal feedback gain from measurements of the cylinder motion. For consistency with the equations provided in the article body, the approach is presented in terms of the exact asymptotic model, the same approach being used in practice with the extended model. Since the system is assumed to evolve on a limit cycle, the evolution equations written in terms of the state vector $\mathbf{Q}_\infty = (|\mathcal{A}_\infty|, |\mathcal{Y}_\infty|, \phi_\infty)^T$ read

$$\mathbf{M}(\mathbf{Q}_\infty, \kappa_\infty) = \mathbf{0}. \tag{A.1}$$

In order to minimize the cost functional defined as

$$\mathcal{J} = -4\omega_s\omega_*^2\gamma|\mathcal{Y}_\infty|^2 + |\kappa_\infty|^2|\mathcal{Y}_\infty|^2, \tag{A.2}$$

we define the Lagrangian

$$\mathcal{L} = \mathcal{J} - \mathbf{Q}^\dagger \cdot \mathbf{M}(\mathbf{Q}_\infty, \kappa_\infty), \tag{A.3}$$

where $\mathbf{Q}_\infty^\dagger = (|\mathcal{A}_\infty|^\dagger, |\mathcal{Y}_\infty|^\dagger, \phi_\infty^\dagger)^T$ is a Lagrange multiplier for the state variables and $\cdot$ refers to the canonical hermitian scalar product in $\mathbb{C}^n$. As is classically done for such minimization problems, we enforce the stationarity of the Lagrangian with respect to the state, control, and adjoint variables, the gradient with respect to any variable s being defined as

$$\frac{\partial \mathcal{L}}{\partial s} \delta s = \lim_{\epsilon \to 0} \frac{\mathcal{L}(s + \epsilon \delta s) - \mathcal{L}(s)}{\epsilon}. \tag{A.4}$$

The gradient of the Lagrangian with respect to the adjoint variables is trivially zero, provided the state equations are satisfied. After some elementary algebraic manipulations, the gradient with respect to the state variables can be written as

$$\frac{\partial \mathcal{L}}{\partial \mathbf{Q}} \delta Q = (\boldsymbol{b} - \mathbf{L}^\dagger(\mathbf{Q}_\infty, \kappa_\infty)\mathbf{Q}^\dagger) \cdot \delta Q, \tag{A.5}$$

with $\boldsymbol{b}$ the array

$$\boldsymbol{b} = \begin{pmatrix} 2|\kappa_\infty|^2|\mathcal{Y}_\infty| \\ -8\omega_s\omega_*^2\gamma|\mathcal{Y}_\infty| \\ 0 \end{pmatrix}, \tag{A.6}$$

and $\mathbf{L}^\dagger$ the adjoint of the linearized evolution operator $\mathbf{L} = \partial\mathbf{M}/\partial\mathbf{Q}$. The latter is given by the 3×3 matrix

$$\begin{aligned}
&\mathbf{L}_{11} = \lambda_r\left(\frac{1}{\mathrm{Re}_*} - \frac{1}{\mathrm{Re}}\right) - 3\mu_r|\mathcal{A}_\infty|^2, && \mathbf{L}_{12} = \tilde{\alpha}_r\cos\phi_\infty + \tilde{\alpha}_i\sin\phi_\infty, \\
&\mathbf{L}_{13} = |\mathcal{Y}_\infty|(\tilde{\alpha}_i\cos\phi_\infty - \tilde{\alpha}_r\sin\phi_\infty), && \mathbf{L}_{21} = \frac{\beta}{\omega_*m}\cos\phi_\infty, \\
&\mathbf{L}_{22} = -\omega s\gamma, && \mathbf{L}_{23} = -\frac{\beta}{\omega_*m}|\mathcal{A}_\infty|\sin\phi_\infty, \\
&\mathbf{L}_{31} = -2\mu_i|\mathcal{A}_\infty| - \frac{1}{|\mathcal{A}_\infty|^2}\mathbf{L}_{13} + \frac{1}{|\mathcal{A}_\infty||\mathcal{Y}_\infty|}\mathbf{L}_{23}, && \mathbf{L}_{32} = \frac{1}{|\mathcal{A}_\infty||\mathcal{Y}_\infty|}\mathbf{L}_{13} - \frac{1}{|\mathcal{Y}_\infty|^2}\mathbf{L}_{23}, \\
&\mathbf{L}_{33} = \frac{|\mathcal{Y}_\infty|}{|\mathcal{A}_\infty|}\mathbf{L}_{12} - \frac{|\mathcal{A}_\infty|}{|\mathcal{Y}_\infty|}\mathbf{L}_{21},
\end{aligned} \tag{A.7}$$

with $\tilde{\alpha} = \alpha + \chi\kappa$. Since there are no derivatives, the adjoint operator is simply $\mathbf{L}^\dagger = \mathbf{L}^T$. Canceling relation (A.5), we obtain that the adjoint variables are solutions of the linear, inhomogeneous problem

$$\mathbf{L}^\dagger(\mathbf{Q}_\infty, \kappa_\infty)\mathbf{Q}_\infty^\dagger = \boldsymbol{b}. \tag{A.8}$$

Finally, the gradients with respect to the control variables are

$$\frac{\partial\mathcal{L}}{\partial\kappa_{r\infty}}\delta\kappa_{r\infty} = \left[-|\mathcal{A}_\infty|^\dagger|\mathcal{Y}_\infty|(\chi_r\cos\phi_\infty + \chi_i\sin\phi_\infty) + \phi_\infty^\dagger\frac{|\mathcal{Y}_\infty|}{|\mathcal{A}_\infty|}(\chi_r\sin\phi_\infty - \chi_i\cos\phi_\infty) + 2\kappa_{r\infty}|\mathcal{Y}_\infty|^2\right]\delta\kappa_{r\infty}, \tag{A.9a}$$

$$\frac{\partial\mathcal{L}}{\partial\kappa_{i\infty}}\delta\kappa_{i\infty} = \left[-|\mathcal{A}_\infty|^\dagger|\mathcal{Y}_\infty|(\chi_r\sin\phi_\infty - \chi_i\cos\phi_\infty) - \phi_\infty^\dagger\frac{|\mathcal{Y}_\infty|}{|\mathcal{A}_\infty|}(\chi_r\cos\phi_\infty + \chi_i\sin\phi_\infty) + 2\kappa_{i\infty}|\mathcal{Y}_\infty|^2\right]\delta\kappa_{i\infty}. \tag{A.9b}$$

In the most general case, the algorithm is initialized from the optimal value computed from the closest set of structural parameters available. If no such optimum exists, then the algorithm simply starts from the unforced case. The gradients (A.9) are then used within a standard conjugate algorithm to iterate the guess until a minimum of the cost functional is reached. It is worth mentioning here that the cost functional is defined on a non-infinite domain of control variables, since only gains yielding positive amplitudes $|\mathcal{A}_\infty|$ and $|\mathcal{Y}_\infty|$ are admissible. Therefore, the minimum can be reached either within, or at the boundary of the domain of definition. The latter domain being not known a priori, we carry out the iterative process until the relative variation in the control variables becomes smaller than 0.01%, the settings yielding negative amplitudes being systematically filtered out. When the minimum is reached within the domain, we check a posteriori that the typical first-order condition is satisfied, i.e. the gradient residual defined by

$$\max\left\{\left|\frac{\partial\mathcal{L}}{\partial\kappa_{r\infty}}\right|, \left|\frac{\partial\mathcal{L}}{\partial\kappa_{i\infty}}\right|\right\}, \tag{A.10}$$

is smaller than 10^{-11}. When the minimum is reached at the boundary, no such condition exists, and we find that the gradient residual varies typically between 10^{-4} and 10^{-8}.

References

Barkley, D., 2006. Linear analysis of the cylinder wake mean flow. Europhysics Letters 75, 750–756.

Bernitsas, M., Ben-Simon, Y., Raghavan, K., Garcia, E., 2009. The vivace converter: model tests at high damping and Reynolds number 10^5. Journal of Offshore Mechanics and Arctic Engineering 131 011102:1–12.

Bernitsas, M., Raghavan, K., Ben-Simon, Y., Garcia, E., 2008. Vivace (vortex induced vibration aquatic clean energy): a new concept in generation of clean and renewable energy from fluid flow. Journal of Offshore Mechanics and Arctic Engineering 130 041101:1–15.

Blevins, R., 1990. Flow-Induced Vibrations. Van Nostrand Reinhold, New York.

Chomaz, J.M., 2005. Global instabilities in spatially developing flows: non-normality and nonlinearity. Annual Review of Fluid Mechanics 37, 357–392.

Gabbai, R., Benaroya, H., 2005. An overview of modeling and experiments of vortex-induced vibration of circular cylinders. Journal of Sound and Vibration 282, 575–616.

Giannetti, F., Luchini, P., 2007. Structural sensitivity of the first instability of the cylinder wake. Journal of Fluid Mechanics 581, 167–197.

Govardhan, R., Williamson, C., 2000. Modes of vortex formation and frequency response of a freely vibrating cylinder. Journal of Fluid Mechanics 420, 85–130.

Gunzburger, M., 1997. Introduction into mathematical aspects of flow control and optimization, in: Lecture Series 1997-05 on Inverse Design and Optimization Methods, Von Kármán Institute for Fluid Dynamics.

Hill, D., 1992. A theoretical approach for analyzing the restabilization of Wakes. Technical Report 103858. NASA.

Kim, J., Bewley, T., 2007. A linear systems approach to flow control. Annual Review of Fluid Mechanics 39, 383–417.
Mathis, C., Provansal, M., Boyer, L., 1984. Bénard von-Kármán instability: an experimental study near the threshold. Journal de Physique Lettres 45, 483–491.
Meliga, P., Chomaz, J.-M., 2011. An asymptotic expansion for the vortex-induced vibrations of a circular cylinder. Journal of Fluid Mechanics 671, 137–167.
Sarpkaya, T., 2004. A critical review of the intrinsic nature of vortex-induced vibrations. Journal of Fluids and Structures 19, 389–447.
Sipp, D., Lebedev, A., 2007. Global stability of base and mean flows: a general approach and its applications to cylinder and open cavity flows. Journal of Fluid Mechanics 593, 333–358.
Williamson, C., Govardhan, R., 2004. Vortex-induced vibrations. Annual Review of Fluid Mechanics 36, 413–455.